HySwash: A hybrid model for nearshore wave processes

Alba Ricondo [*], Laura Cagigal, Beatriz Pérez-Díaz, Fernando J. Méndez

Geomatics and Ocean Engineering Group, Departamento de Ciencias y Técnicas Del Agua y Del Medio Ambiente, E.T.S.I.C.C.P, Universidad de Cantabria, Santander, Spain

ARTICLE INFO

ABSTRACT

Climate change-induced sea level rise and increasing storm severity are significant stressors that threaten the livability of coastal areas worldwide. This research presents a site-specific metamodel based on SWASH (Simulating WAves till SHore) numerical model simulations that aim at simplifying in a fast and efficient manner the prediction of hydrodynamic variables along cross-shore profiles. To accomplish this, a large synthetic database of offshore wave and sea level conditions is created and downscaled using numerical modeling together with sampling, selection, and interpolation techniques. All these mathematical methods permit to replace the computationally intensive cost of classical dynamical downscaling. In addition, the metamodel uses dimensionality reduction techniques that allow to account for a comprehensive analysis of the primary patterns governing the coastal hydrodynamic behavior. The proposed tool has been numerically validated in three different idealized coral reef profiles, showing good skill at reproducing the spatial evolution of wave setup, wave heights associated with different frequency bands, and wave runup. The flexibility and robustness of the method make it very convenient for being used in coastal risk assessments, early warning systems, or climate change projections.

1. Introduction

Coastal flooding results from the combination of multivariate atmospheric and oceanographic dynamics that interact with the coastal topography. As sea level and storm frequency and intensity are expected to rise along numerous coastlines throughout the world (Oppenheimer et al., 2022), coastal flooding will also increase both in frequency and severity (Vitousek et al., 2017). In this context, it is crucial to effectively predict coastal flooding and provide the necessary tools to assist adaptation strategies to coastal communities and policymakers. These predictive tools should be able to forecast the local waves and water levels and their nearshore transformation to the shoreline. Commonly, phase-resolving numerical wave models have been employed for simulating the complex nearshore hydrodynamics of specific storm events (Wandres et al., 2020). Although they accurately reproduce the main physical processes, these models are computationally costly, posing a limitation on the ability to forecast conditions with limited resources. Alternatively, hybrid models have emerged to complement process-based wave numerical models by incorporating statistical methods that minimize the computational effort. Recent works make use of hybrid methods for downscaling tropical cyclone-induced waves (van Vloten et al., 2022), ocean regular wave climate to coastal areas (Camus

et al., 2011a; Gouldby et al., 2014; Ricondo et al., 2023), or transferring wave and water levels from nearshore to the flooding extent (Gainza et al., 2018; Rueda et al., 2019).

Due to the ecological importance, inherent vulnerability, and urgent response needed in coral reef-lined coasts (Winter et al., 2020), there have been several efforts to parameterize combinations of fringing coral reef profiles (e.g., beach slope, reef flat width, and fore reef slope) and hydrodynamic conditions (e.g., water depth, wave height, and wave period) to forecast wave-induced flooding. Callaghan et al. (2018) used a Bayesian belief network to link reef, wave, and wind parameters with the beach toe significant wave height. Yao et al. (2021) employed the multi-layer perception neural network to predict tsunami-like solitary wave run-up over fringing reefs. Amores et al. (2022) developed a model-based parameterization for wave setup, Pearson et al. (2017) developed BEWARE, a model based on Bayesian neural networks to forecast the top 2% wave runup based on an extensive synthetic database, and Rueda et al. (2019) later used the same synthetic database as BEWARE to develop a hybrid method, named HyCReWW, based on Radial Basis Functions (RBFs). However, the complex hydrodynamics occurring in coral reefs and the highly diverse characteristics of coastal profiles in terms of shape, slope, and roughness still present a challenge when forecasting wave transformation without generating an extensive

---

Fig. 1. Sketch of the methodology.

presented, HySwash, is built on combining sampling, clustering, and interpolation techniques with a high-fidelity hydrodynamic model. The statistical techniques aim at overcoming the computational burden of dynamical downscaling by minimizing the number of needed numerical simulations. We present its application to 3 different coral reef schematic profiles and explore its capability in estimating several surf-zone quantities.

The paper is organized as follows. Section 2 presents the HySwash methods into four subsections "Beach morphology and hydrodynamic forcing", "Numerical Modeling", "Reconstruction", and "Numerical Validation". Section 3 presents the results of the hydrodynamic reconstruction and replicability of the metamodel to different profile settings, and conclusions are covered in Section 4.

2. HySwash method

The HySwash methodology workflow is illustrated in Fig. 1, and the methods are detailed in the following sub-sections. Firstly, a synthetic database of nearshore wave conditions is created using the Latin Hypercube Sampling (LHS) technique, and further selection of a smaller number of representative forcing conditions is achieved with the Maximum Dissimilarity Algorithm (MDA, Camus et al., 2011b) (Section 2.1). These cases are dynamically downscaled using SWASH (Simulating WAves till SHore) (version 8.01) (Zijlema et al., 2011) (Section 2.2). The output variables are subjected to Principal Component Analysis (PCA) to reduce their dimensionality while preserving the spatial structure; and finally, Radial Basis Functions are used to create an interpolation function from new unmodeled nearshore conditions to the prediction of surf-zone hydrodynamics (Section 2.3). The method is numerically validated using a k-fold cross-validation in Section 2.4.

2.1. Beach morphology and hydrodynamic forcing

The proposed metamodel is a wave-induced flooding predictive tool valid for any coastal morphology (i.e., sandy, or reef-fronted coastlines). Due to the inherent vulnerability of reef ecosystems and their urgent need to improve the understanding of their hydrodynamic processes, we present the application of HySwash to reef morphologies. In contrast to typical sandy beaches, wave processes in coral reefs present a strongly non-linear behavior of impinging waves (Lee and Black, 1979). Wave breaking is the dominant mechanism driving flow over the reef flat (Lowe et al., 2009) while it accounts for the majority of energy dissipation at the reef crest (Brander et al., 2004; A. C. Péquignet et al., 2011). As waves enter the shallower water in the reef flat, wave attenuation caused by bottom friction becomes increasingly important. Wave transformation from the reef crest to the shoreline is characterized by the evolution of the frequency spectra from high-frequency dominance to low-frequency dominance. In order to study the wave transformation
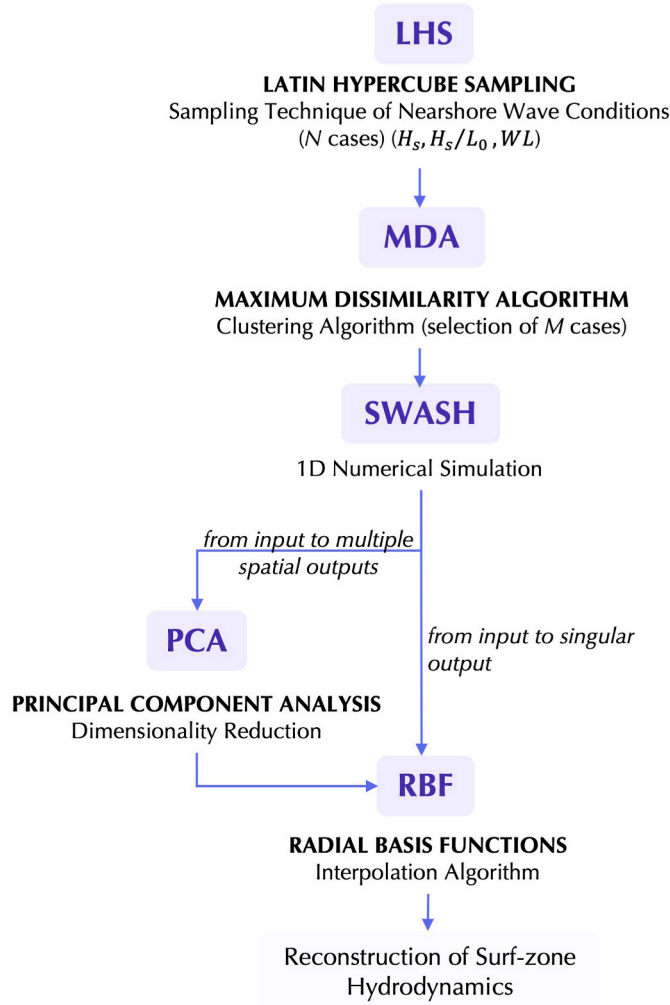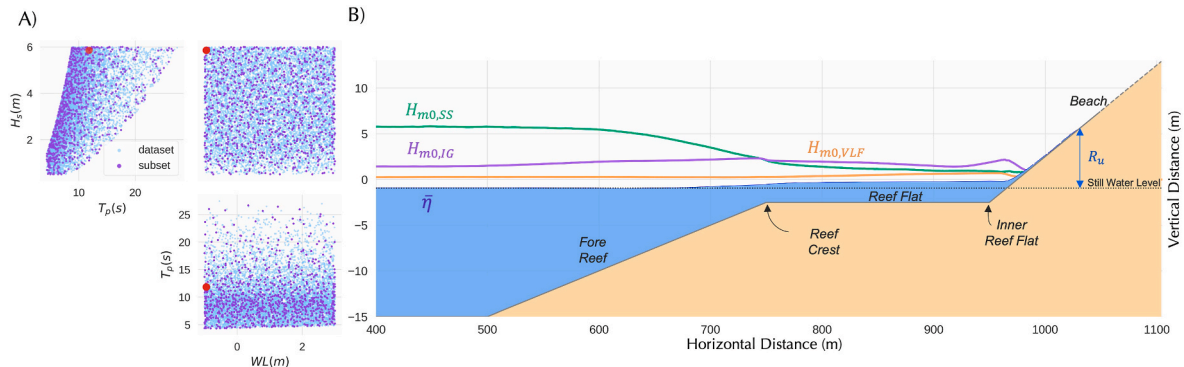
database of hydrodynamic combinations or simplifying the morphology. In this respect, Scott et al. (2020) make use of clustering techniques to simplify the singularity of global reef profiles. Even so, these approaches require some simplification of reef morphology and focus on wave runup or wave setup as flooding proxies.

Here, we present a novel one-dimensional hydrodynamic hybrid model that aims to extend previous efforts on estimating surf-zone hydrodynamics on specific coastal morphologies. The hybrid model

Fig. 2. Hydrodynamic forcing and reef morphology. A) MDA-design cases (violet data points) distributed over the LHS-synthetic dataset (light blue data points). A random subset case is highlighted in red ($H_s = 5.8$ m, $T_p = 12$ s, $WL = -0.9$ m), and the corresponding SWASH modeled output is shown in (B). B) Reef profile morphology along with the computed SWASH outputs (R_u, $\bar{\eta}$, $H_{m0,SS}$, $H_{m0,IG}$ and $H_{m0,VLF}$) of the individual case highlighted in (A).

Table 1
Hydrodynamic parameters and their range of values.

Parameter	Symbol	Units	Ranges
Offshore water level	WL	m	(-1, 3)
Offshore significant wave heigh	H_s	m	(0.5, 6)
Offshore wave steepness	H_s/L_0	–	(0.005, 0.05)

processes of a reef profile but keep it general enough, we have defined an idealized horizontal reef top profile that follows the simplest geomorphological characteristics of reef profiles measured on several Pacific atolls and fringing reefs (Gourlay, 1996; Quataert et al., 2015). The proposed reef is presented in Fig. 2B. The idealized reef profile is characterized by a constant fore reef slope of 1/20, horizontal reef flat width of 200 m, and beach slope of 1/10. The reef flat is 2.5 m below the mean sea level, and the beach crest elevation was fixed at 30 m to avoid wave overtopping and focus the analysis on the run-up excursion over the beach slope. In order to place the wavemaker boundary away from the area of interest, a 500 m long flat region at 15 m depth has been included before the fore reef.

Waves and tidal oscillations are the most relevant predictive offshore hydrodynamic variables for flooding. These variables include short-term (i.e., local wind waves, distant-source swells) and long-term (i.e., tides, surges, mean sea level, increasing sea level) processes. Based on previous hydrodynamic modeling studies (Pearson et al., 2017), the metamodel parameters that define the offshore wave and water level conditions are the significant wave height (H_s), wave steepness (H_s/L_0), and offshore water level (WL). We produce physically plausible combinations of wave heights and periods when sampling the wave steepness instead of wave periods. We define the wave sea-states at the beginning of the profile as single-peaked unidirectional TMA spectrum, which is a generalized version of the JONSWAP (Joint North Sea Wave Project) offshore spectra valid for arbitrary-depth waters. Bouws et al. (1985) initially proposed the TMA spectrum to modify the spectral shape as water depth reduces from deep to shallow waters, limiting the energy of the low-frequency waves. The expression for the TMA spectrum can be obtained by multiplying the JONSWAP spectrum by a function of wave frequency and water depth. Therefore, considering the initial depth of 15 m, we transform the JONSWAP spectrum to a TMA spectrum and finally rescaled it to maintain the energy.

To generate a comprehensive range of forcing conditions and extreme events that have never been measured but are likely to happen, we use the LHS technique (McKay et al., 1979). This sampling method can generate near-random samples from a multivariate space. The LHS first requires choosing the number of sample points (N) to obtain. Every dimension is then divided into N equal-probability intervals. The individual samples are randomly generated and placed only once in each axis-aligned hyperplane. This corresponds to one sample in each row and column for a two-dimensional LHS. In comparison to random sampling, the LHS tends to require significantly smaller sample sizes and yields samples that accurately reflect the underlying distribution. We set the LHS to create N combinations of the primary offshore parameters $V = \{H_s, H_s/L_0, WL\}$. In order to evenly cover the multidimensional space, we set $N = 10,000$. The parameter ranges are established based on existing field measurements (Quataert et al., 2015). Table 1 summarizes the hydrodynamic offshore parameters and their range of values. The H_s range from 0.5 to 6 m, H_s/L_0 is bounded by a minimum steepness value of 0.005 and a maximum of 0.05, and WL ranges from −1 to 3 m. As the further use of PCA requires a shared spatial domain, the range of WL is desired to ensure that the reef flat remains submerged during low tide and does not dry out.

After populating the multidimensional parameter space with N combinations, we use the MDA to select a minimum number of representative conditions needed to train the metamodel (M cases). The MDA algorithm was first proposed by Camus et al. (2011b) for the study of multivariate wave climate and widely used in a variety of metamodels

afterwards (Camus et al., 2011a; Gainza et al., 2018; Gouldby et al., 2014; Ricondo et al., 2023; van Vloten et al., 2022). The algorithm is implemented on the normalized input data vectors (V') as:

$$V' = \frac{V - \min(V)}{\max(V) - \min(V)} \tag{1}$$

The seed to the algorithm is the dataset case with the greatest Euclidean distance to the rest M-1 vectors. Iteratively, the following subset cases are selected from the input dataset as the most dissimilar point to the pre-selected MDA-increasing cases. When the number of cases in the subset reaches the desired M value, the algorithm finishes. This number of cases will be dependent on the reef morphology, hydrodynamic forcing, and variables to estimate and must be determined for each specific location. Thus, the number of cases is determined by fitting the metamodel with increasing M values and evaluating its performance by the root-mean-square error (RMSE) using the k-fold algorithm (details in Section 3). The initial LHS samples ($N = 10,000$) and the selected MDA subset for $M = 1000$, are presented in Fig. 2A. Note that to make the figure easier to interpret, the peak period is represented instead of the wave steepness.

2.2. Numerical modeling

The wave transformation along the coral reef was simulated using one-dimensional SWASH simulations. SWASH is a non-hydrostatic, phase-resolving wave model capable of simulating waves from deep waters to the shoreline, modeling wave breaking, bottom friction, wave-induced setup and runup, and the generation and propagation of infragravity waves. The accuracy of the model is comparable to that of lower-order Boussinesq models and has been widely used for modeling wave dynamics and inundation on sandy beaches and coral reefs (Liu et al., 2021; Rijnsdorp et al., 2012; Zijlema, 2012; Zijlema et al., 2011).

From the selection of M offshore wave parameters, a sequence of hourly-varying irregular unidirectional water elevation is created to feed SWASH simulations. In non-hydrostatic mode, SWASH was run along the cross-shore transects with constant horizontal resolution determined through a number of points per wavelength. In order to accurately resolve the wave transformation in the shallowest area, 60 nodes were chosen to define the wavelengths at 1 m depth. The duration of the simulation was set to 4 h with 15 additional minutes of spin-up. One hour may be enough for obtaining stable statistics, but extending it to 4 h, as in Pearson et al. (2017), increases the number of spectral components and enables a reduction in uncertainty related to the initial random phases. The bottom friction is included in the simulation with a constant Manning coefficient of 0.002. Note that the calibration of this parameter is not the purpose of this work. The entire set of sea states has been modeled with two vertical layers of equal thickness. However, introducing more vertical layers in the numerical setup should be considered for real case applications to coral reefs to better resolve the linear frequency dispersion (Fiedler et al., 2019; Henderson et al., 2022; Ruju et al., 2019).

The primary SWASH output variables stored are the water level time series along the profile and vertical water elevation on the beach. From these variables, several magnitudes have been computed as indicative of relevant hydrodynamic processes on the reef. The mean wave setup ($\bar{\eta}$) is calculated by averaging the water level and subtracting the offshore water level. From the water level time series, the individual wave heights are obtained by zero-up-crossing, obtaining the root-mean-square wave height (H_{rms}) as a measure of average wave conditions. Since low frequency waves play an important role in flooding of reef-lined coast induced by resonance modes (Gawehn et al., 2016), we include frequency band components as predicted variables. To compute them, the power spectra water level signal is divided into its sea-swell (SS), infragravity (IG), and very low frequency (VLF) components by bandpass filtering. This allows for the identification of the significant
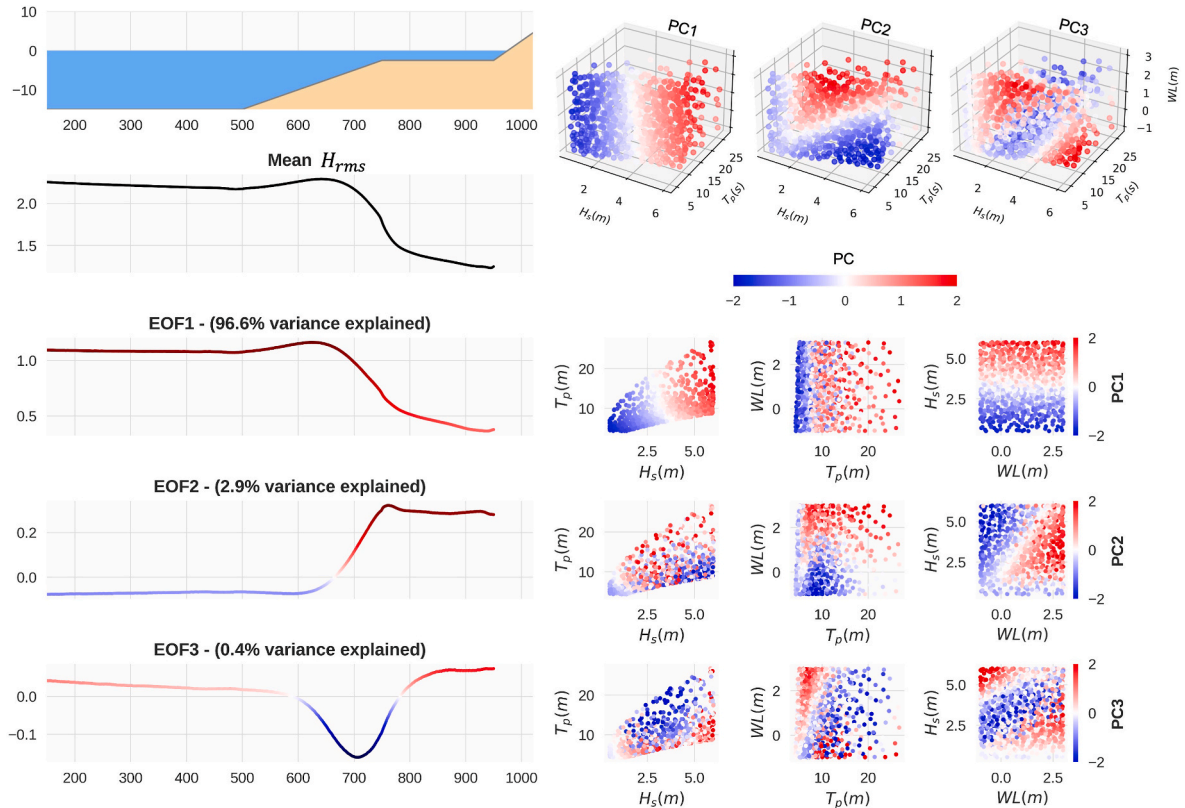
Table 2
Summary of non-hydrostatic output parameters.

Parameter	Symbol	Units
Mean wave setup	$\overline{\eta}$	m
Root-mean-square wave height	H_{rms}	m
Significant sea/swell wave height (0.04–1 Hz)	$H_{m0,SS}$	m
Significant infragravity wave height (0.004–0.04 Hz)	$H_{m0,IG}$	m
Significant very low frequency wave height (0.001–0.004 Hz)	$H_{m0,VLF}$	m
Runup on beach slope (2% exceedance value)	$R_{2\%}$	m
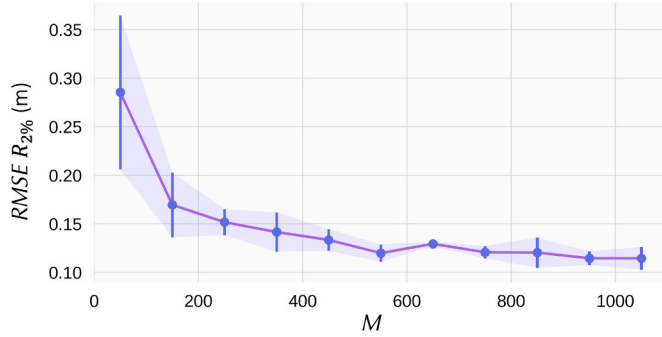
Fig. 3. K-fold cross validation on the $R_{2\%}$ as a function of the number of cases that set up the metamodel. The point is the mean RMSE value, and the error bars are the standard deviation of the k-folds.

wave height at sea-swell frequencies (0.04–1 Hz) ($H_{m0,SS}$), significant wave height at infragravity frequencies (0.004–0.04 Hz) ($H_{m0,IG}$), and significant wave height at very low frequencies (0.001–0.004 Hz)

($H_{m0,VLF}$). Finally, the vertical runup has been calculated as the value only exceeded by 2% of the waves ($R_{2\%}$). Table 2 summarizes the non-hydrostatic output quantities obtained from the water level and run-up signal processing.

2.3. Reconstruction

From the *M*-selected forcing inputs and their *M*-transformed SWASH-1D outputs, it is possible to approximate the underlying spatial relationship between input and output with an interpolation surface. This interpolation surface enables the estimation of output variables for unmodeled input cases. We use RBF interpolation, as it is especially suitable when dealing with highly dimensional and irregularly distributed data (Alfeld, 1989). This interpolation technique has been previously used in several metamodels with accurate interpolation skills (Camus et al., 2011a; Gouldby et al., 2014; Ricondo et al., 2023). For a new vector of input parameters *V*, the RBF interpolation returns a univariate metamodel output $y(V)$. This is the case of the $R_{2\%}$ or any other SWASH output evaluated at a certain location in the profile. When attempting to reconstruct the evolution of spatial fields of wave height or setup, we would need to fit as many RBFs as target locations in the profile. As this involves a significant increase in the computational time and possible inconsistencies between adjacent points, we make use of the PCA technique before the RBF interpolation as it reduces the dimensionality of the dataset and preserves the spatial patterns. PCA has been widely used in many fields, such as climatology to identify dominant variability patterns (Camus et al., 2013; Robinet et al., 2020). By projecting the original data onto a new space, PCA captures the maximum variance in the sample data. This new space is formed by the eigenvectors (empirical orthogonal functions, EOFs) and the transformed components of the original data over the EOFs (PCs). The EOFs

Fig. 4. The first three components of the PCA (99.8% variance explained) applied to H_{rms}. The left side panel presents the cross-shore reef morphology; mean H_{rms} and EOFs. The right panel displays the corresponding PCs. The amplitudes of the PCs are firstly projected on a 3D scatter of the 750 parameters of the forcing variables and subsequently in 2D scatters. The PC cases scattered in red positively amplify the corresponding EOF, while the blue points amplify it negatively. The EOFs are colored in red (positive values) and blue (negative values), following their magnitudes to facilitate their interpretation.
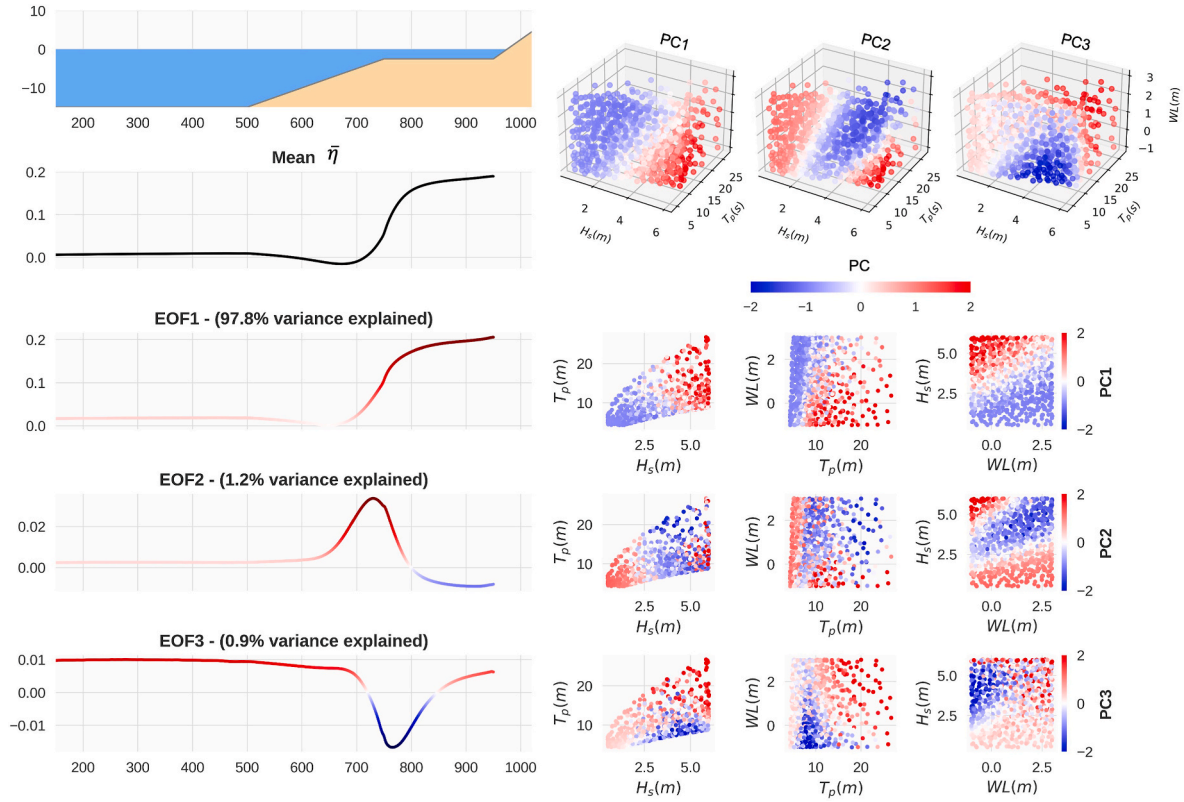
Fig. 5. The first 3 components of the PCA (99.8% variance explained) applied to $\bar{\eta}$. The left side panel presents the cross-shore reef morphology, the average $\bar{\eta}$ and EOFs, and the right panel the PCs. The color rules are analogous to those in Fig. 4.

capture the major oscillation patterns, while the PCs represent their variability along the *M* cases. As the EOFs are rated in increasing order of explained variance, the dimensionality reduction is given by selecting the number of EOFs that define a desired percentage of explained variance. Here, we have decided to keep the principal modes that explain the 99.8% of variance. The number of more relevant principal components will depend on the complexity of the patterns explored. After applying the PCA to the SWASH output quantity $y(x; H_s, T_p, WL)$ of dimensions P x *M*, where P is the number of spatial locations (x) along the profile, the originally modeled output corresponding to each case can be obtained as a linear combination of EOFs and PCs following:

$$y\left(x; H_s, T_p, WL\right) = \bar{y}(x) + \sum_{n=1}^{M} EOF_n(x) \bullet PC_n\left(H_s, T_p, WL\right) \quad (2)$$

where $\bar{y}(x)$ is the mean of the output variable along the *M* cases. As the interpolated metamodel output must be univariate, we use RBF interpolation to reconstruct the reduced set of principal components (PCs), one by one. The general RBF interpolation surface is of the form:

$$RBF(V) = p(V) + \sum_{i=1}^{M} a_i \Phi\left(\|V - V_i\|\right) \quad (3)$$

where $p(V)$ is a linear polynomial with coefficients $b = \{b_0, b_1, ..., b_m\}$, m is the dimension of the input forcing parameters (in this case 3), $\| \bullet \|$ is the Euclidean norm, and Φ is Gaussian functions with a user-specified parameter (ε) that modifies the shape of the distributions. Here, we adopt the algorithm proposed by Rippa (1999) to obtain the optimal ε parameter. The coefficients a_i and b_i need to be found for *C* principal components that explain the defined variance ($PC_1, PC_2...PC_C$). Therefore, the estimated spatial field of the response function is:

$$y\left(x; H_s, T_p, WL\right) \approx \bar{y}(x) + EOF_1(x) \bullet PC_1\left(H_s, T_p, WL\right) + \cdots$$
$$+ EOF_C(x) \bullet PC_C\left(H_s, T_p, WL\right) \quad (4)$$

Once the coefficients are obtained, the multidimensional RBF interpolation allows the replacement of the SWASH model to obtain the principal components of the different output quantities along the domain for unmodeled forcing conditions.

2.4. Numerical validation

Finally, we evaluate the performance of the mathematical model on a k-fold cross validation (k = 5). The *M* subset cases are divided into k folds. Iteratively, the model is trained on the k-1 folds and tested on the remaining one. To determine the minimum number of cases needed to set up the metamodel, the k-fold validation was firstly used on the $R_{2\%}$. The k iterations are repeated over an increasing number of *M* cases, from a minimum value of 50 to a maximum of 1000. This has required having the first 1000 MDA cases numerically simulated. The RMSE is obtained from each k iteration, and the M value as a performance metric. This yields a mean RMSE and standard deviation for each *M* case. Fig. 3 displays the RMSE of the $R_{2\%}$ reconstruction as a function of *M*. The metamodel accuracy with higher *M* cases is observed by decreasing mean RMSE and associated uncertainty. At this point, a decision on the *M* value that allows to obtain the required level of accuracy on the variable needs to be made. As the mean and standard deviation get minimal at $M = 750$ (RMSE $R_{2\%} = 0.12$ m), we decided to set the metamodel with the first 750 MDA cases. The remaining hydrodynamic variables have also been subject to the k-fold, and the results indicate that, for the same number of cases, they are significantly more straightforward to predict than the $R_{2\%}$. Thus, $M = 750$ is optimum for applying the hybrid method to every output magnitude.
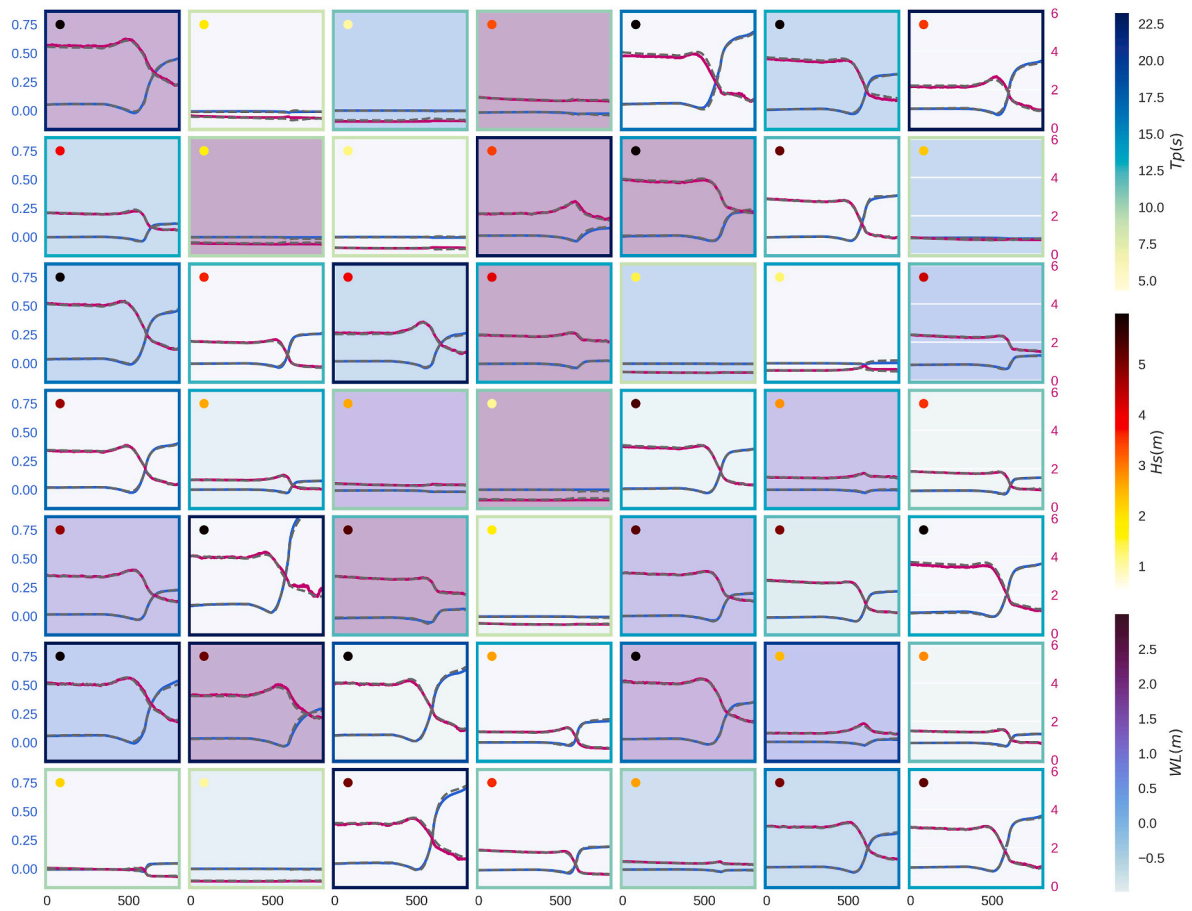
Fig. 6. Comparison of modeled (solid line) versus reconstructed (dashed line) H_{rms} (pink axis on the right) and η_{setup} (blue axis on the left) for the first 49 cases of the MDA. The background color indicates the *WL*, the edgecolor the T_p and the point the H_s.

3. Results

Once the optimal number of cases (*M*) to minimize the error is determined, the metamodel will be fully trained. This training involves performing the *M*-SWASH simulations, conducting PCA and RBF fitting, and evaluating the agreement with the k-fold cross validation. Each simulation took 9 min to run in an Ubuntu (x86-64) PC, using up to eight 3 GHz Intel i7-9700 processors and 32 GB of RAM, and the final fitting of the RBF surfaces was 5 min. Once this is accomplished, the response to un-modeled forcing conditions from regional/global wave models can be obtained in seconds. The efficiency of this metamodel allows to reproduce different time scales that range from downscaling large hindcast records, forecasting short-term conditions, or predicting flooding driven by long-term sea level rise projections in a timely manner.

3.1. Hydrodynamics exploration through PCA

Before the RBF interpolation, the PCA is used to reduce the dimensionality of the spatial outputs ($\overline{\eta}$; $H_{rms}, H_{m0,SS}, H_{m0,IG}, H_{m0,VLF}$) as detailed in Section 2.3 as opposed to the $R_{2\%}$, where the reconstruction is made directly using RBF interpolation. Following Equation (1), after applying the PCA to the *M* vectors of a certain metric to convert them to the PCA space, it is possible to revert to the original space by adding to the mean of the variable every EOF component multiplied by its corresponding PC amplitude. Note that the PCA results will be specific to the topo-bathymetry of the study case. The interpretability of the resulting EOFs and PCs is a second concern in the hybrid model development. However, there is a greater possibility that the resulting EOFs will have a

physical interpretation when the physical relationship between variables is linear, and the input data have been properly preprocessed and normalized. The principal components resulting from the PCA applied on the $\overline{\eta}$ and H_{rms} are depicted respectively in Figs. 4 and 5. For both $\overline{\eta}$ and H_{rms}, only three principal components can explain 99.8% of the variance, with the first one explaining more than 96%. The PC values associated with the 750 MDA cases and to every EOF for H_{rms}, are represented in 3D scatters in Fig. 4. This representation aids the visualization of how well PCA can identify the main oscillation modes as a function of the tridimensional combination of forcing parameters. As can be seen in the average H_{rms} pattern of Fig. 4, the mean spatial model remains constant before the fore reef slope. As waves move through the fore reef slope, waves shoal up before abruptly decreasing as they break at the crest. Incident high frequency waves may be fully dissipated by breaking or reflected on the reef edge, while a reduced energy percentage is transferred towards the reef flat. The first oscillation mode (EOF1) can be associated with the time-varying breakpoint mechanism located at the reef crest. Looking at the PC amplitudes of this first mode, higher H_s and T_p correspond to positive PC1 values that amplify this primary pattern of strong dissipation caused by depth-limited breaking at the reef crest. Since this principal component accounts for 96.6% of the variance, the majority of the modeled cases are highly influenced by this pattern. The combined effect of H_s and WL is explained by the second principal component (EOF2), explaining the 2.9% of the variance. This second mode responds to waves that shoal up over the reef flat when large WL (red PC2) or break on the fore reef if shallow water depth. After shoaling or breaking, wave energy over the reef flat remains constant. The third principal component explains very little variance (0.4 %) and presents a strong shoaling effect from the fore slope toe to
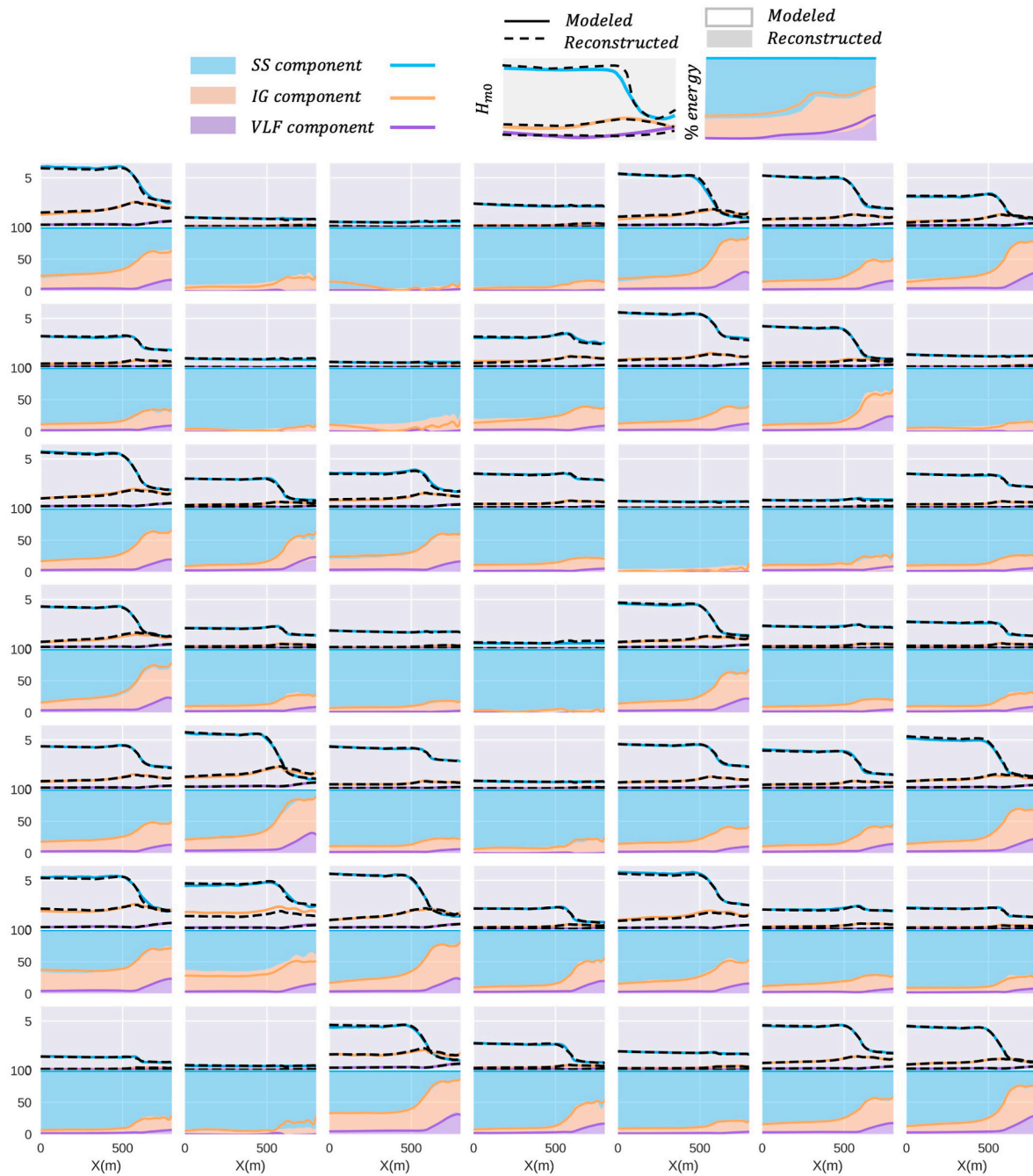
Fig. 7. Comparison of modeled versus reconstructed $H_{m0,SS}$, $H_{m0,IG}$ and $H_{m0,VLF}$ of the first 49 cases of the MDA. The upper panels plot the modeled (black dashed line) versus reconstructed (colored solid line) H_{m0} of each frequency band. The lower panels represent the relative contribution of each frequency band to the total energy measured as H_{m0}^2.

the reef crest before breaking for long period high energetic wave conditions and low tide or directly breaking with no shoaling for low energy waves and high tide.

Wave force acting in a shoreward direction applies a force on the water column that produces water level variations to compensate for the radiation stress gradients. Breaking waves produce an increase in the mean surface water level, and shoaling waves decrease. Therefore, from the PCA applied to the $\overline{\eta}$, similar patterns to those described for the H_{rms} (Fig. 4) can be appreciated. The EOF1 presents a similar pattern to the average $\overline{\eta}$, explaining 97.8% of the variance. This evolution remains relatively constant across the reef flat, with a larger increase towards the shore. The variability of PC1 among the 750 cases reflects that wave setup over the reef increases with increasing H_s and T_p. Wave setup is

also larger during low water levels than during high water levels. The second and third oscillation modes have much smaller oscillations in magnitude. The second principal component is modulated by H_s and WL. When the water depth at the reef flat is low (WL < 1), and the incident wave height is large ($H_{rms} > 4$), the mode represents no gradual shoaling process, and breaking occurs directly. As WL increases, the shoaling effect becomes increasingly relevant up to a H_{rms} local maxima (minimum $\overline{\eta}$), after which waves break. Finally, the third oscillation mode primarily responds to the wave steepness and WL. The mode is amplified for the highest-steepness incident waves (large wave heights with short periods) and lower water levels, evidencing a breaking mechanism at X = 700 and wave setup over the reef flat. Conversely, gentle-steepness waves do not break, and the shoaling produces a
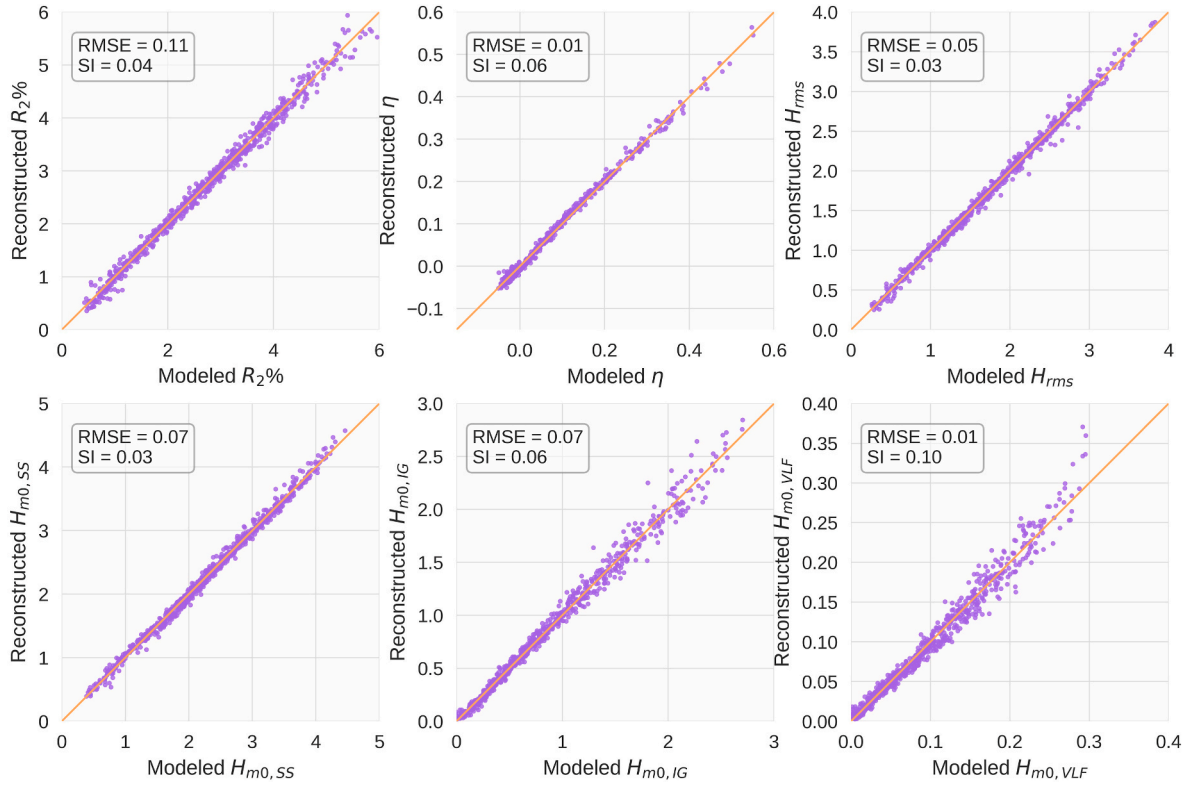
Fig. 8. Scatter validation of the output magnitudes $\bar{\eta}, H_{rms}, H_{m0,SS}, H_{m0,IG}, H_{m0,VLF}, R_{2\%}$ in meters. Except for $R_{2\%}$, the magnitudes are evaluated at the reef crest (X = 750 m).
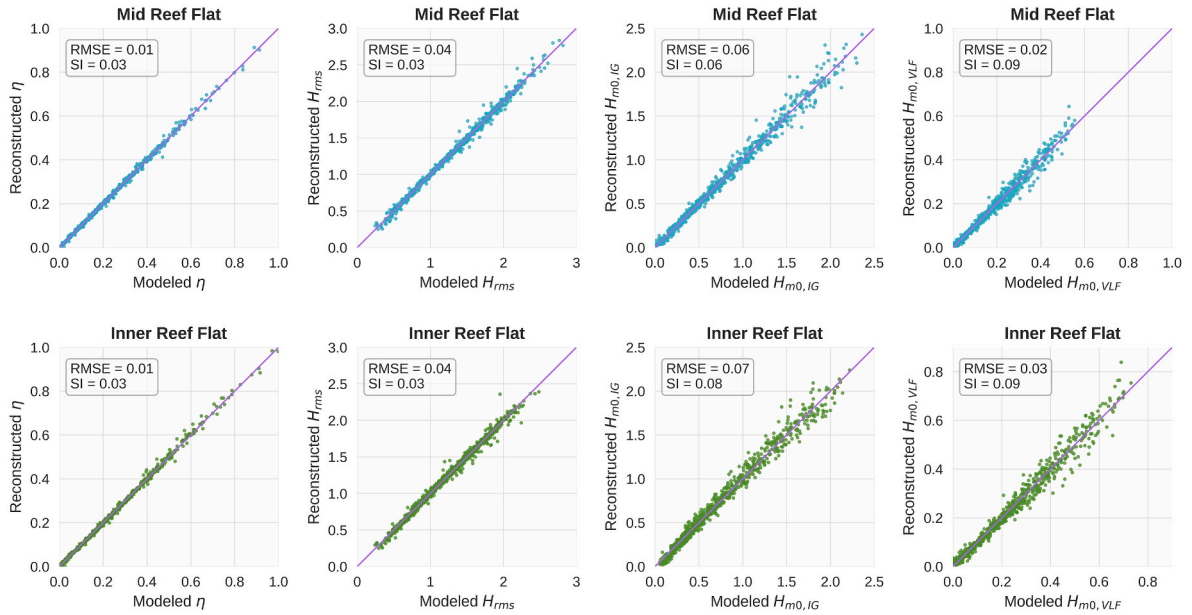

Fig. 9. Comparison of modeled versus reconstructed $\bar{\eta}, H_{rms}, H_{m0,IG}$ and $H_{m0,VLF}$ in meters for the mid reef flat (X = 850 m) and inner reef flat (X = 950 m).

decrease in wave setup on the reef flat.

3.2. Nearshore hydrodynamics reconstruction

In this section, the metamodel performance reconstructing the pre-defined output variables on the idealized reef profile proposed (RP1, see Fig. 2) is discussed. Fig. 6 presents the modeled versus reconstructed H_{rms} and $\bar{\eta}$ for the first 49 MDA cases, which are the most dissimilar. The

larger $\bar{\eta}$ differences in these first cases are located in the reef flat and correspond to cases of low offshore water depth combined with high H_s and T_p. For these cases, the reconstructed $\bar{\eta}$ is slightly underestimated. Overall, the agreement between modeled and reconstructed H_{rms} and $\bar{\eta}$ values is quite positive for the entire cross-shore profile.

In addition, the ability of HySwash to estimate the spectral transformation of waves along the profile is explored by its capability to reconstruct the $H_{m0,SS}$, $H_{m0,IG}$ and $H_{m0,VLF}$ spatial evolution. Fig. 7
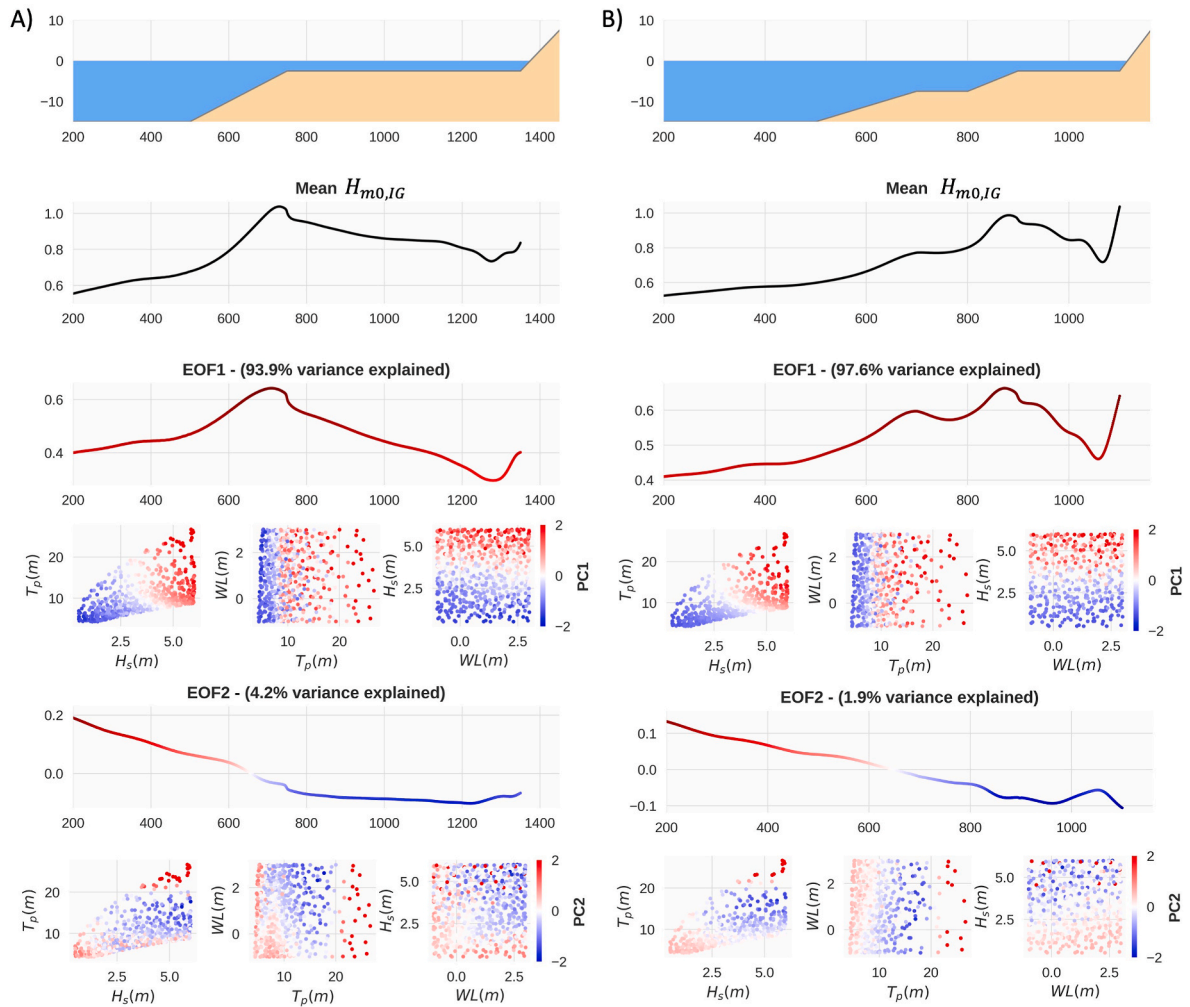
Fig. 10. Reef profiles definitions (RP2 in (A) and RP3 in (B)) and first two principal components on $H_{m0,IG}$.

Table 3
Detailed geometry of the three idealized reef profiles.

Reef Profile	Fore Reef Slope	Offshore Reef Flat Width	Onshore Reef Flat Width	Beach Slope
RP1	1/20	200	–	1/10
RP2	1/20	600	–	1/10
RP3	1/20	100	200	1/10

presents the comparison between the modeled and reconstructed H_{m0} frequency bands for the first 49 MDA cases. The total energy is measured by $H_{m0}{}^2$, and energy corresponding to each frequency component is defined by $(H_{m0,SS}/H_{m0})^2$, $(H_{m0,IG}/H_{m0})^2$, and $(H_{m0,VLF}/H_{m0})^2$. Moving towards the surf zone, the energy pattern shows that the sea-swell energy band diminishes, and the lower frequency harmonic components emerge. While at the fore reef, SS energy dominates over the $H_{m0,IG}$ and $H_{m0,VLF}$, it gradually increases by the mid to the inner reef flat. At the inner reef, the contribution to the overall sea state by the SS waves is small compared to the IG and VLF waves. This behavior of the modeled spectral transformation agrees with previous studies and observations on reef environments (e.g. Battjes et al., 2004; Péquignet et al., 2014; Young, 1989). From the comparison of modeled versus reconstructed H_{m0} and energy evolution, it can be noted that the metamodel does good work in reconstructing the energy transfer from high to low frequency components. This is particularly relevant since IG and VLF oscillations are crucial in the sediment transport and thus in shaping the

morphological features of the coral reefs (Masselink et al., 2019; Pomeroy et al., 2015). These low-frequency modes have also been observed to control extreme flooding events in low-lying atolls (Ford et al., 2012; Merrifield et al., 2014).

To quantify the level of agreement, the RMSE and scatter index (SI) error statistics are displayed in Fig. 8 for different cross-shore locations (for $\bar{\eta}$, H_{rms}, $H_{m0,SS}$, $H_{m0,IG}$, $H_{m0,VLF}$, $R_{2\%}$ at the reef crest) and Fig. 9 (for $\bar{\eta}$; H_{rms}, $H_{m0,IG}$, $H_{m0,VLF}$ at the mid reef and inner reef flat). The overall performance is very positive, with RMSE below 0.11 m. The best performance achieved in the reconstruction is for the $\bar{\eta}$ (RMSE = 0.01 m and SI = 0.06), while the error rate is higher for increasing non-linear variables. Equally, the error is higher when higher non-linear wave dynamic interactions occur along the profile. This can be seen as RMSE is higher for the mid reef flat than for the inner reef (Fig. 9) and for the reef crest than for the mid reef. In overall, the comparison indicates good predictive skill for every output quantity defined.

3.3. Metamodel sensitivity to coastal morphology

Reef and sandy profiles are very variable, and their morphology largely influences the wave breaking and transformation processes (Yao et al., 2019). The reef morphology described in Fig. 2 is characteristic of fringing reef profiles that present a relatively narrow reef flat (<300 m). In order to assess the predictive capabilities of HySwash for different coastal morphologies, two more idealized reef profiles have been defined (see Fig. 10). The detailed geometry of the three idealized reef
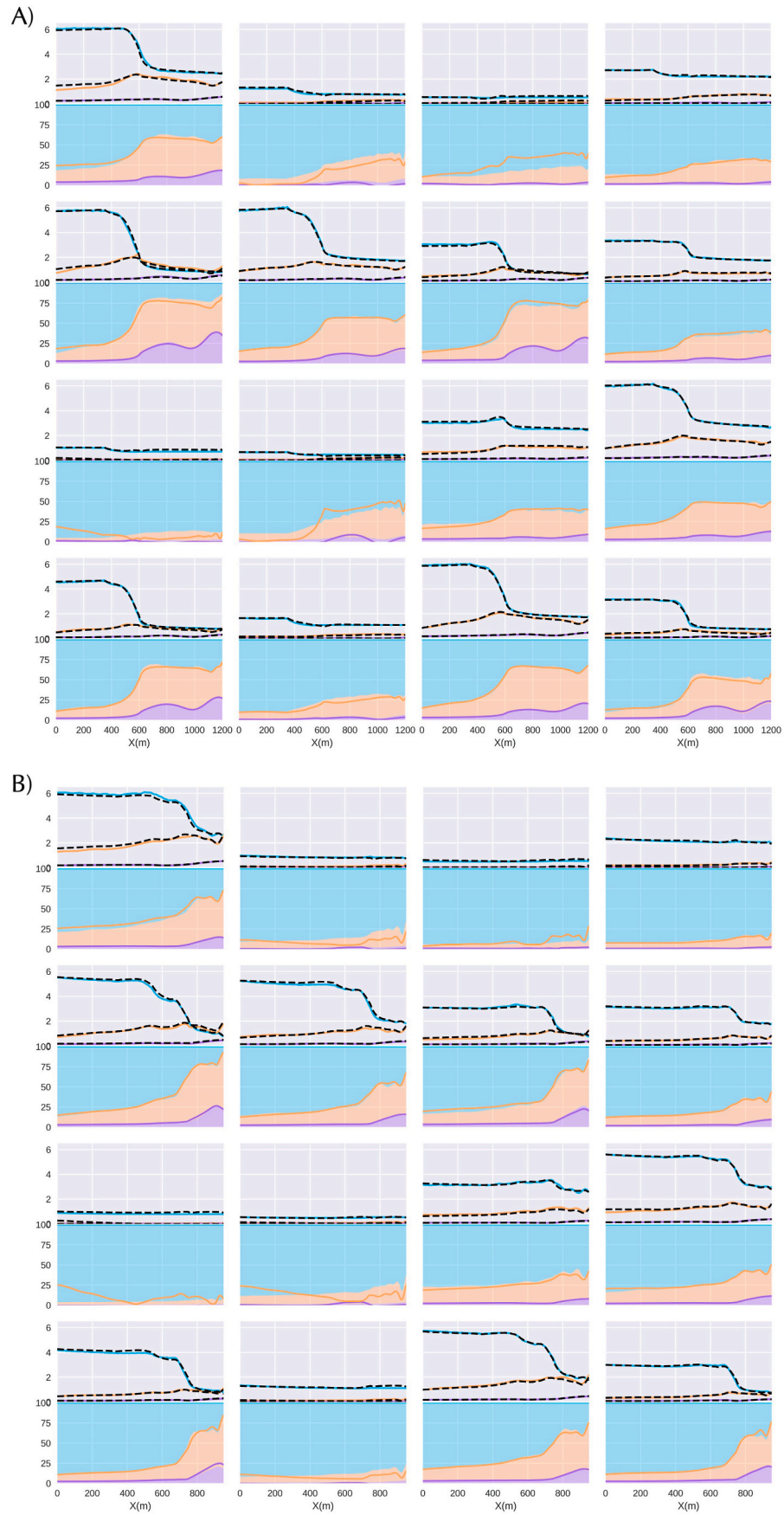
Fig. 11. Comparison of modeled versus reconstructed $H_{m0,SS}$, $H_{m0,IG}$ and $H_{m0,VLF}$ for RP2(A) and RP3(B).

Table 4
Summary of HySwash M design cases and error metrics for the three profiles defined measured at the reef crest (X = 750 m).

	M	$R_{2\%}$	RMSE (m)				
			$\bar{\eta}$	H_{rms}	$H_{m0,SS}$	$H_{m0,IG}$	$H_{m0,VLF}$
RP1 (200 m reef flat)	750	0.11	0.01	0.05	0.07	0.07	0.01
RP2 (600 m reef flat)	600	0.10	0.01	0.04	0.05	0.06	0.02
RP3 (double reef flat)	500	0.14	0.02	0.07	0.11	0.07	0.01

profiles is presented in Table 3. The first proposed reef profile (RP2) has a reef length of 600 m, longer than PR1 while maintaining the same fore reef and beach. The second reef profile (RP3) presents double reef flats with an offshore reef measuring 100 m and a nearshore reef of 200 m.

For example, Fig. 10 displays the first two principal components resulting from the PCA on the $H_{m0,IG}$. The PCA domain covers the cross-shore profile from X = 150 m to the inner reef flat, with the first principal component explaining more than 93% of the variance in both cases. As IG energy release is mainly driven by the breaking point mechanism (Pomeroy et al., 2012), the mean $H_{m0,IG}$ reveals that the short-period waves in RP2 first break at the reef crest generating a local maximum of 1 m on average. The mean $H_{m0,IG}$ evolution pattern and first oscillation mode (EOF1) of both profiles properly illustrate the short wave breaking and IG release points. For the RP3, the first two break-points are located at both reef crests, with a higher peak at the nearshore reef crest as it is at a shallower depth. As higher wave energy reaches the reef and propagates across it in RP3, the innermost wave breaking point is located further away from the coast than in RP2, with a maximum $H_{m0,IG}$ released of 1 m on average. PC1 is very similar for RP2 and RP3, showing that incident H_s and T_p control the IG energy along the reef in that greater offshore wave power led to larger low-frequency waves over the reef flat. The tidal dependency appreciated for $\bar{\eta}$ and H_{rms} in Fig. 4 (EOF1) and Fig. 5 (EOF2), is not as well recognized here. Common to both profiles (RP2 and RP3), the second principal component (EOF2) exhibits a progressive decay all along the reef profile. The corresponding PC values indicate that this pattern is frequency dependent, with the highest positive amplitudes given by T_p higher than 20 s. We may link this principal component with the second IG generation mechanism, the bound long waves. For T_p ranging from 6 to 20 s, energy transfer to the IG band gradually increases as waves move to nearshore depths. This can be seen in the blue PC2 values that reverse the EOF2 pattern. T_p higher than 20 s or lower than 6 s responds to a decreasing evolution of the IG energy. This may be related to the breaking of individual waves within the large period wave groups ($T_p > 20$ s) for an initial depth of 15 m and the numerical dispersion of waves linked to the short-period wave groups ($T_p < 6$ s).

The PCA has been presented on the $H_{m0,IG}$ and results from the k-fold reconstruction of the low-frequency components for RP2 and RP3 are presented in Fig. 11 for the first 16 MDA cases of both HySwash setups. Noticeably, the VLF energy is higher in PR2 than in PR3. Narrow steep fore reef slopes are particularly prone to flooding caused by resonant modes or VLF energy amplification (Cheriton et al., 2016). An overall summary of the performance of HySwash on the three reef profiles defined is provided In Table 4. Compared to the RP1, fewer SWASH simulations are required to achieve a similar order of accuracy in the prediction of $R_{2\%}$ for the RP2 ($M = 600$), and even less for profile 3 ($M = 500$). Further work could be done to determine which coastal morphologies are most vulnerable to flooding or how spectral transformation is driven across the profile using the PCA technique. Although we have defined different reef morphologies by varying the reef flat characteristics, the fore reef and beach slope are essential in modeling reef hydrodynamics and subsequent flooding.

4. Conclusions

A fast and efficient hybrid method is proposed to estimate surf-zone hydrodynamics given the offshore wave and sea-level conditions and the cross-shore profile morphology. The hybrid model, named HySwash, is built on the use of the SWASH 1-D numerical model and statistical techniques (LHS, MDA, PCA, RBF) that permit to reduce the number of scenarios to simulate. The LHS technique allows to create a synthetic database of forcing variables that account for mean and extreme conditions. This is especially important since it enables the training of the metamodel to cover potential future events that may still need to be measured. In addition, by combining PCA and RBF techniques, we can leverage the strengths of both statistical methods to achieve efficient and accurate reconstructions in high-dimensional datasets. On this basis, it has been proven that HySwash can estimate the wave runup, wave setup, or wave height evolution along the profile for a far lower computational cost than the commonly used dynamic downscaling. In addition, the PCA offers a powerful tool to investigate complex dynamics and identify the primary variables influencing its oscillations.

In the current research, only numerical validation of the metamodel has been carried out through the k-fold cross validation. Note that for real case applications, instrumental validation will be needed to calibrate and validate the numerical model. The metamodel has been proven to accurately reproduce key reef hydrodynamics on three different reef profile morphologies covering the range of possible offshore conditions. Despite being a location-specific metamodel, its capacity to reconstruct hydrodynamic variables in seconds, numerically simulating a reduced set of synthetic forcing conditions, makes it a powerful tool.

The methodology developed in this study will contribute to a better understanding of the physical processes governing surf-zone hydrodynamics. HySwash can be integrated as a fast and efficient tool to inform early warning systems or to assess the potential impacts of climate change, coastal development (e.g., beach stability, design of coastal structures), and other coastal activities.

CRediT author statement

Alba Ricondo: Methodology, Formal analysis, Software, Visualization, Writing - Original Draft.
Laura Cagigal: Methodology, Writing- Reviewing and Editing.
Beatriz Perez: Conceptualization, Writing- Reviewing and Editing.
Fernando J. Méndez: , Conceptualization, Methodology, Supervision, Writing- Reviewing and Editing, Funding acquisition.

Declaration of competing interest

The authors declare that they have no known competing financial interests or personal relationships that could have appeared to influence the work reported in this paper.

Data availability

Data will be made available on request.

References

Alfeld, P., 1989. Scattered data interpolation in three or more variables. In: Mathematical Methods in Computer Aided Geometric Design, vol. 5. Academic Press, Inc. https://doi.org/10.1016/b978-0-12-460515-2.50005-6.

Amores, A., Marcos, M., Le Cozannet, G., Hinkel, J., 2022. Coastal flooding and mean sea-level rise allowances in atoll island. Sci. Rep. 12 (1) https://doi.org/10.1038/S41598-022-05329-1.

Battjes, J.A., Bakkenes, H.J., Janssen, T.T., van Dongeren, A.R., 2004. Shoaling of subharmonic gravity waves. J. Geophys. Res.: Oceans 109 (2). https://doi.org/10.1029/2003JC001863.

Bouws, E., Gunther, H., Rosenthal, W., Vincent, C.L., 1985. Similarity of the wind wave spectrum in finite depth water: 1. Spectral form. J. Geophys. Res.: Oceans 90 (C1), 975–986. https://doi.org/10.1029/JC090IC01P00975.

Brander, R.W., Kench, P.S., Hart, D., 2004. Spatial and temporal variations in wave characteristics across a reef platform, Warraber Island, Torres Strait, Australia. Mar. Geol. 207 (1–4), 169–184. https://doi.org/10.1016/j.margeo.2004.03.014.

Callaghan, D.P., Baldock, T.E., Shabani, B., Mumby, P.J., 2018. Communicating physics-based wave model predictions of coral reefs using Bayesian belief networks. Environ. Model. Software 108, 123–132. https://doi.org/10.1016/j.envsoft.2018.07.021.

Camus, P., Mendez, F.J., Medina, R., 2011a. A hybrid efficient method to downscale wave climate to coastal areas. Coast. Eng. 58 (9), 851–862. https://doi.org/10.1016/j.coastaleng.2011.05.007.

Camus, P., Mendez, F.J., Medina, R., Cofiño, A.S., 2011b. Analysis of clustering and selection algorithms for the study of multivariate wave climate. Coast. Eng. 58 (6), 453–462. https://doi.org/10.1016/j.coastaleng.2011.02.003.

Camus, P., Mendez, F.J., Medina, R., Tomas, A., Izaguirre, C., 2013. High resolution downscaled ocean waves (DOW) reanalysis in coastal areas. Coast. Eng. 72, 56–68. https://doi.org/10.1016/j.coastaleng.2012.09.002.

Cheriton, O.M., Storlazzi, C.D., Rosenberger, K.J., 2016. Observations of wave transformation over a fringing coral reef and the importance of low-frequency waves and offshore water levels to runup, overwash, and coastal flooding. J. Geophys. Res.: Oceans 121 (5), 3121–3140. https://doi.org/10.1002/2015JC011231.

Fiedler, J.W., Smit, P.B., Brodie, K.L., McNinch, J., Guza, R.T., 2019. The offshore boundary condition in surf zone modeling. Coast. Eng. 143 (April 2018), 12–20. https://doi.org/10.1016/j.coastaleng.2018.10.014.

Ford, M.R., Becker, J.M., Merrifield, M.A., 2012. Reef flat wave processes and excavation pits: observations and implications for majuro atoll, Marshall Islands, 10.2112/JCOASTRES-D-12-00097.1, 29(3), 545–554. https://doi.org/10.2112/JCOASTRES-D-12-00097.1.

Gainza, J., Rueda, A., Camus, P., Tomás, A., Méndez, F.J., Sano, M., Tomlinson, R., 2018. A meta-modelling approach for estimating long-term wave run-up and total water level on beaches. J. Coast. Res. 34 (2), 475–489. https://doi.org/10.2112/JCOASTRES-D-16-00198.1.

Gawehn, M., van Dongeren, A., van Rooijen, A., Storlazzi, C.D., Cheriton, O.M., Reniers, A., 2016. Identification and classification of very low frequency waves on a coral reef flat. J. Geophys. Res.: Oceans 121 (10), 7560–7574. https://doi.org/10.1002/2016JC011834.

Gouldby, B., Méndez, F.J., Guanche, Y., Rueda, A., Mínguez, R., 2014. A methodology for deriving extreme nearshore sea conditions for structural design and flood risk analysis. Coast. Eng. 88, 15–26. https://doi.org/10.1016/J.COASTALENG.2014.01.012.

Gourlay, M.R., 1996. Wave set-up on coral reefs. 2. set-up on reefs with various profiles. Coast. Eng. 28 (1–4), 17–55. https://doi.org/10.1016/0378-3839(96)00009-9.

Henderson, C.S., Fiedler, J.W., Merrifield, M.A., Guza, R.T., Young, A.P., 2022. Phase resolving runup and overtopping field validation of SWASH. Coast. Eng. 175 (July 2021), 104128 https://doi.org/10.1016/j.coastaleng.2022.104128.

Lee, T.T., Black, K.P., 1979. Energy spectra of surf waves on a coral reef. Proc. Coast. Eng. Conf. 1, 588–608. https://doi.org/10.9753/icce.v16.33.

Liu, Y., Liao, Z., Fang, K., Li, S., 2021. Uncertainty of wave runup prediction on coral reef-fringed coasts using SWASH model. Ocean. Eng. 242, 110094 https://doi.org/10.1016/J.OCEANENG.2021.110094.

Lowe, R.J., Falter, J.L., Monismith, S.G., Atkinson, M.J., 2009. Wave-driven circulation of a coastal reef-lagoon system. J. Phys. Oceanogr. 39 (4), 873–893. https://doi.org/10.1175/2008JPO3958.1.

Masselink, G., Tuck, M., McCall, R., van Dongeren, A., Ford, M., Kench, P., 2019. Physical and numerical modeling of infragravity wave generation and transformation on coral reef platforms. J. Geophys. Res.: Oceans 124 (3), 1410–1433. https://doi.org/10.1029/2018JC014411.

McKay, M.D., Beckman, R.J., Conover, W.J., 1979. Comparison of three methods for selecting values of input variables in the analysis of output from a computer code. Technometrics 21 (2), 239–245. https://doi.org/10.1080/00401706.1979.10489755.

Merrifield, M.A., Becker, J.M., Ford, M., Yao, Y., 2014. Observations and estimates of wave-driven water level extremes at the Marshall Islands. Geophys. Res. Lett. 41 (20), 7245–7253. https://doi.org/10.1002/2014GL061005.

Oppenheimer, M., Glavovic, B.C., Hinkel, J., van de Wal, R., Magnan, A.K., Abd-Elgawad, A., Cai, R., Cifuentes-Jara, M., DeConto, R.M., Ghosh, T., Hay, J., Isla, F.,

Marzeion, B., Meyssignac, B., Sebesvari, Z., 2022. Sea level rise and implications for low-lying islands, coasts and communities. In: Pörtner, H.-O., Roberts, D.C., Masson-Delmotte, V., Zhai, P., Tignor, M., Poloczanska, E., Mintenbeck, K., Alegría, A., Nicolai, M., Okem, A., Petzold, J., Rama, B., Weyer, N.M. (Eds.), The Ocean and Cryosphere in a Changing Climate. Cambridge University Press, pp. 321–446. https://doi.org/10.1017/9781009157964.006.

Pearson, S.G., Storlazzi, C.D., van Dongeren, A.R., Tissier, M.F.S., Reniers, A.J.H.M., 2017. A bayesian-based system to assess wave-driven flooding hazards on coral reef-lined coasts. J. Geophys. Res.: Oceans 122 (12), 10099–10117. https://doi.org/10.1002/2017JC013204.

Péquignet, A.C., Becker, J.M., Merrifield, M.A., Boc, S.J., 2011. The dissipation of wind wave energy across a fringing reef at Ipan, Guam. Coral Reefs 30 (Suppl. 1), 71–82. https://doi.org/10.1007/s00338-011-0719-5.

Péquignet, A.C.N., Becker, J.M., Merrifield, M.A., 2014. Energy transfer between wind waves and low-frequency oscillations on a fringing reef, Ipan, Guam. J. Geophys. Res.: Oceans 119 (10), 6709–6724. https://doi.org/10.1002/2014JC010179.

Pomeroy, A., Lowe, R., Symonds, G., Van Dongeren, A., Moore, C., 2012. The dynamics of infragravity wave transformation over a fringing reef. J. Geophys. Res.: Oceans 117 (C11), 11022. https://doi.org/10.1029/2012JC008310.

Pomeroy, A.W.M., Lowe, R.J., Van Dongeren, A.R., Ghisalberti, M., Bodde, W., Roelvink, D., 2015. Spectral wave-driven sediment transport across a fringing reef. Coast. Eng. 98, 78–94. https://doi.org/10.1016/J.COASTALENG.2015.01.005.

Quataert, E., Storlazzi, C., Van Rooijen, A., Cheriton, O., Van Dongeren, A., 2015. The influence of coral reefs and climate change on wave-driven flooding of tropical coastlines. Geophys. Res. Lett. 42 (15), 6407–6415. https://doi.org/10.1002/2015GL064861.

Ricondo, A., Cagigal, L., Rueda, A., Hoeke, R., Storlazzi, C.D., Méndez, F.J., 2023. HyWaves: hybrid downscaling of multimodal wave spectra to nearshore areas. Ocean Model. 102210 https://doi.org/10.1016/J.OCEMOD.2023.102210.

Rijnsdorp, D.P., Smit, P.B., Zijlema, M., 2012. NON-HYDROSTATIC modelling of infragravity waves using SWASH. Coast. Eng. Proc. 1 (33), 27. https://doi.org/10.9753/icce.v33.currents.27 currents.

Rippa, S., 1999. An algorithm for selecting a good value for the parameter c in radial basis function interpolation. Adv. Comput. Math. 11 (2), 193–210. https://doi.org/10.1023/A:1018975909870, 1999 11:2.

Robinet, A., Castelle, B., Idier, D., Harley, M.D., Splinter, K.D., 2020. Controls of local geology and cross-shore/longshore processes on embayed beach shoreline variability. Mar. Geol. 422, 106118 https://doi.org/10.1016/J.MARGEO.2020.106118.

Rueda, A., Cagigal, L., Pearson, S., Antolínez, J.A.A., Storlazzi, C., van Dongeren, A., Camus, P., Mendez, F.J., 2019. HyCReWW: a hybrid coral reef wave and water level metamodel. Comput. Geosci. 127 (February 2018), 85–90. https://doi.org/10.1016/j.cageo.2019.03.004.

Ruju, A., Lara, J.L., Losada, I.J., 2019. Numerical assessment of infragravity swash response to offshore wave frequency spread variability. J. Geophys. Res.: Oceans 124 (9), 6643–6657. https://doi.org/10.1029/2019JC015063.

Scott, F., Antolinez, J.A.A., McCall, R., Storlazzi, C., Reniers, A., Pearson, S., 2020. Hydro-morphological characterization of coral reefs for wave runup prediction. Front. Mar. Sci. 7 https://doi.org/10.3389/FMARS.2020.00361.

van Vloten, S.O., Cagigal, L., Rueda, A., Ripoll, N., Méndez, F.J., 2022. HyTCWaves: a Hybrid model for downscaling Tropical Cyclone induced extreme Waves climate. Ocean Model. 178 https://doi.org/10.1016/J.OCEMOD.2022.102100.

Vitousek, S., Barnard, P.L., Fletcher, C.H., Frazer, N., Erikson, L., Storlazzi, C.D., 2017. Doubling of coastal flooding frequency within decades due to sea-level rise. Sci. Rep. 7 (1), 1–9. https://doi.org/10.1038/s41598-017-01362-7, 2017 7:1.

Wandres, M., Aucan, J., Espejo, A., Jackson, N., De Ramon N'Yeurt, A., Damlamian, H., 2020. Distant-source swells cause coastal inundation on Fiji's coral coast. Front. Mar. Sci. 7 (July) https://doi.org/10.3389/fmars.2020.00546.

Winter, G., Storlazzi, C., Vitousek, S., van Dongeren, A., McCall, R., Hoeke, R., Skirving, W., Marra, J., Reyns, J., Aucan, J., Widlansky, M., Becker, J., Perry, C., Masselink, G., Lowe, R., Ford, M., Pomeroy, A., Mendez, F., Rueda, A., Wandres, M., 2020. Steps to develop early warning systems and future scenarios of storm wave-driven flooding along coral reef-lined coasts. Front. Mar. Sci. 7 (March), 1–8. https://doi.org/10.3389/fmars.2020.00199.

Yao, Y., Yang, X., Lai, S.H., Chin, R.J., 2021. Predicting tsunami-like solitary wave run-up over fringing reefs using the multi-layer perceptron neural network. Nat. Hazards 107 (1), 601–616. https://doi.org/10.1007/s11069-021-04597-w.

Yao, Y., Zhang, Q., Chen, S., Tang, Z., 2019. Effects of reef morphology variations on wave processes over fringing reefs. Appl. Ocean Res. 82, 52–62. https://doi.org/10.1016/j.apor.2018.10.021.

Young, I.R., 1989. Wave transformation over coral reefs. J. Geophys. Res.: Oceans 94 (C7), 9779–9789. https://doi.org/10.1029/JC094IC07P09779.

Zijlema, M., 2012. Modelling wave transformation across a fringing reef using SWASH. Coast. Eng. Proc. 1 (33), 26. https://doi.org/10.9753/icce.v33.currents.26 currents.

Zijlema, M., Stelling, G., Smit, P., 2011. SWASH: an operational public domain code for simulating wave fields and rapidly varied flows in coastal waters. Coast. Eng. 58 (10), 992–1012. https://doi.org/10.1016/J.COASTALENG.2011.05.015.